

UCSF

UC San Francisco Previously Published Works

Title

Noninvasive, Targeted Creation of Neuromyelitis Optica Pathology in AQP4-IgG Seropositive Rats by Pulsed Focused Ultrasound.

Permalink

<https://escholarship.org/uc/item/8h17v0xb>

Journal

Journal of neuropathology and experimental neurology, 78(1)

ISSN

0022-3069

Authors

Yao, Xiaoming
Adams, Matthew S
Jones, Peter D
[et al.](#)

Publication Date

2019

DOI

10.1093/jnen/nly107

Peer reviewed

Noninvasive, Targeted Creation of Neuromyelitis Optica Pathology in AQP4-IgG Seropositive Rats by Pulsed Focused Ultrasound

Xiaoming Yao, MD, PhD, Matthew S. Adams, PhD, Peter D. Jones, BS, Chris J. Diederich, PhD, and Alan S. Verkman, MD, PhD

Abstract

Neuromyelitis optica spectrum disorders (herein called NMO) is an autoimmune disease of the CNS characterized by astrocyte injury, inflammation, and demyelination. In seropositive NMO, immunoglobulin G autoantibodies against aquaporin-4 (AQP4-IgG) cause primary astrocyte injury. A passive transfer model of NMO was developed in which spatially targeted access of AQP4-IgG into the CNS of seropositive rats was accomplished by pulsed focused ultrasound through intact skin. Following intravenous administration of microbubbles, pulsed ultrasound at 0.5 MPa peak acoustic pressure was applied using a 1 MHz transducer with 6-cm focal length. In brain, the transient opening of the blood-brain barrier (BBB) in an approximately prolate ellipsoidal volume of diameter ~ 3.5 mm and length ~ 44 mm allowed entry of IgG-size molecules for up to 3–6 hours. The ultrasound treatment did not cause erythrocyte extravasation or inflammation. Ultrasound treatment in AQP4-IgG seropositive rats produced localized NMO pathology in brain, with characteristic astrocyte injury, inflammation, and demyelination after 5 days. Pathology was not seen when complement was inhibited, when non-NMO human IgG was administered instead of AQP4-IgG, or in AQP4-IgG seropositive AQP4 knock-out rats. NMO pathology was similarly created in cervical spinal cord in seropositive rats. These results establish a noninvasive, spatially targeted model of NMO in rats, and demonstrate that BBB permeabilization, without underlying injury or inflammation, is sufficient to create NMO pathology in AQP4-IgG seropositive rats.

Key Words: Aquaporin-4, Blood-brain barrier, Focused ultrasound, Neuromyelitis optica, Rats, Spinal cord.

INTRODUCTION

Neuromyelitis optica spectrum disorders (herein called NMO) is an autoimmune disease of the central nervous system (CNS) characterized by inflammation and demyelination in spinal cord, optic nerve, and brain. In seropositive NMO circulating immunoglobulin G autoantibodies against water channel aquaporin-4 (AQP4), called AQP4-IgG, bind to AQP4 on astrocytes and cause injury by complement and cellular cytotoxicity mechanisms (1–4). Secondary inflammation and injury to oligodendrocytes result in demyelination and neurological deficit. Various other mechanisms may contribute to NMO disease pathogenesis such as antibody-dependent cellular cytotoxicity, complement bystander injury, sensitized T cells, and others (5–10).

Animal models of NMO are needed to investigate NMO disease pathogenesis mechanisms and to test therapeutics (reviewed in Refs. [11–15]). The hallmarks of NMO pathology include astrocyte injury with loss of astrocyte markers AQP4 and glial fibrillary acidic protein (GFAP), an inflammatory response with granulocyte infiltration and microglial activation, centrovacular deposition of activated complement, blood-brain barrier (BBB) disruption, and demyelination (1, 3, 4, 16–18). Passive-transfer models of seropositive NMO, in which AQP4-IgG is administered directly into brain and cerebrospinal fluid, have recapitulated some features of NMO pathology (18–24). However, NMO pathology is not seen when rodents are made seropositive for AQP4-IgG (25, 26), which is consistent with human data that NMO patients can be AQP4-IgG seropositive for many years without neurological symptoms (27). Mild and variable NMO pathology has been created in AQP4-IgG seropositive rats by invasive CNS injury (25) or by maneuvers causing generalized inflammation (23, 28–30) to allow entry of circulating AQP4-IgG into the CNS.

The goal of this study was to develop a noninvasive approach to produce spatially targeted NMO pathology in AQP4-IgG seropositive rats without immune modulation. Another goal was to test the hypothesis that BBB permeabilization is sufficient to create NMO pathology in seropositive rats. Building on prior work showing efficacy and safety of pulsed focused ultrasound with microbubble cavitation to transiently permeabilize the BBB (31–35) and the blood-spinal cord barrier (36, 37), here we adapted the focused ultrasound

From the Department of Medicine and Physiology (XY, ASV); and Thermal Therapy Research Group, Department of Radiation Oncology, University of California, San Francisco, California (MSA, PDJ, CJD).

Send correspondence to: Alan S. Verkman, MD, PhD, Department of Medicine and Physiology, University of California, San Francisco, 513 Parnassus Ave, San Francisco, CA 94143-0521; E-mail: alan.verkman@ucsf.edu

This work was supported by grants EY13574, EB00415, and DK72517 from the National Institutes of Health, and a grant from the Guthy-Jackson Charitable Foundation.

The authors have no duality or conflicts of interest to declare.

approach to deliver circulating AQP4-IgG into rat CNS. The technical details were optimized to produce robust NMO pathology in brain and spinal cord of AQP4-IgG seropositive rats following a single exposure to pulsed focused ultrasound and microbubble injection.

MATERIALS AND METHODS

Chemicals and Antibodies

Purified recombinant AQP4-IgG (rAb-53) was provided by Dr Jeffrey Bennett (Univ. Colorado, Denver) and (non-NMO) pooled human IgG (hIgG), as control, was purchased from Pierce Biotechnology (Rockford, IL). Some studies were done using an Fc hexamer complement inhibitor (Comp_{inh}) as reported (5), which inhibits the classical complement pathway by >98% for 8–12 hours after intravenous administration. Optison albumin-coated perflutren protein-type A microbubbles (2–4.5 μ m diameter, half-time 2.5–4.5 minutes) were purchased from GE Healthcare (Milwaukee, WI). All reagents were prepared in phosphate-buffered saline. Unless otherwise specified all chemicals were purchased from Sigma-Aldrich (St. Louis, MO).

Rats

Sprague-Dawley rats were purchased from Charles River Lab (Wilmington, MA). Experiments were done using weight-matched rats (~250 g), age 7–9 weeks. AQP4 knockout (AQP4^{-/-}) rats in a Sprague-Dawley background were generated using CRISPR-Cas9 technology as described in Ref. (38). Rats were maintained in air-filtered cages and fed normal rat chow in the University of California, San Francisco (UCSF) Animal Care facility. Procedures were approved by the UCSF Institutional Animal Care Use Committee (IACUC) (approval number AN108551).

Instrumentation and Transducer Characterization

A spherically focused ultrasound transducer (model A392S-SU, Olympus, Webster, TX) with 39-mm diameter and 60-mm focal length operating at a frequency of 1.0 MHz was used to generate the acoustic field. The transducer was driven by an arbitrary function waveform generator (33220 A Agilent Technologies, Palo Alto, CA) through a 50-dB power amplifier (240 L ENI, Inc., Rochester, NY). The focal pressure magnitudes and acoustic field patterns were measured using a calibrated acoustic hydrophone (0.5-mm diameter, HNR-500, Onda Corporation, Sunnyvale, CA) mounted on a 3-axis automated translational stage in front of the transducer in a degassed deionized water tank. The beam measurements were performed following standard procedures using pulsed burst mode, with 100 cycle burst count and 1 kHz repetition rate. Hydrophone output voltage was measured with a digital oscilloscope. Beam profiles in scanning plane transverse to and along the axis of the transducer were measured using 0.5 mm transverse and 1 mm longitudinal step sizes. Net applied electrical power was measured using a power meter and a 40-dB dual directional coupler, and levels required to achieve

0.1–1.0 MPa peak negative pressure in water were measured. In a separate setup, to estimate acoustic attenuation by the rat skull and spinal column, ex vivo experiments were done using an excised portion of an adult rat skull or spinal column as described in Refs. (37, 39). Briefly, the excised skull was enclosed in a cylindrical tissue holder with thin polyethylene membranes on both sides and suspended in the water tank at the focal point between the transducer and hydrophone (0.2-mm diameter, HNP-0200, Onda Corp., Sunnyvale, CA). The transmission loss was estimated using insertion loss techniques, measuring the pressure difference between free-field and presence of skull or spine.

Setup for Ultrasound Treatment of Rats

As diagrammed in Figure 1A, the ultrasound transducer was mounted on a stereotaxic instrument (Model 902 Dual, KOPF, Tujunga, CA) with precision 3D adjustment in position and orientation. To assist the alignment of the beam focal zone with the targeted rat brain region, a custom 3D-printed conical adapter (Zortrax M200 3D printer) was attached to the transducer during positioning. This adapter featured a narrow pointer tip that was registered with the transducer focal position, and could be removed prior to sonication to avoid affecting the nominal beam profile. A separate manipulator was used for positioning of the acoustic coupling reservoir, consisting of an open-top thin polyethylene bag containing deionized, degassed water at room temperature. Coupling of the bag to the rat skin was achieved using compression and ultrasound gel (Scan Ultrasound Gel, Parker Laboratories, Fairfield, NJ). Once the ultrasound transducer was positioned within the reservoir, any bubbles adhering to the surface of the transducer were carefully removed and confirmed by direct visualization prior to sonication.

BBB Permeabilization in Rats

Rats were anesthetized using ketamine (100 mg/kg) and xylazine (10 mg/mL). Hair on the targeted area (head or cervical spine dorsum) was removed using an electric razor followed by depilatory cream (Nair lotion). The femoral vein was cannulated using PE-10 tubing for delivery of microbubbles, antibodies and other compounds. For BBB studies, rats were immobilized on the stereotaxic frame and (without incision) the Lambda landmark was located as the cross-point of the inter-aural line and sagittal suture midline of the skull, and the Bregma was located as 9.0 mm anterior to Lambda on the midline (for ~250 g rats, *The Rat Brain in Stereotaxic Coordinates* [40]). The acoustic focal point was manually positioned 2.5 mm lateral to the midline, 4 mm posterior to the Bregma, and 3 mm beneath the skin. In some studies, the control right hemisphere was exposed to ultrasound first, and then the left hemisphere immediately following intravenous injection of 5–8 $\times 10^8$ /mL (0.4 mL/kg body weight) microbubbles. Just prior to injection and ultrasound treatment the microbubbles were activated by vigorous shaking per manufacturer's instructions.

For most experiments ultrasound parameters were: 10 ms pulse length, 1 Hz pulse repetition rate, and 2 minutes duration. Power settings corresponding to peak-negative

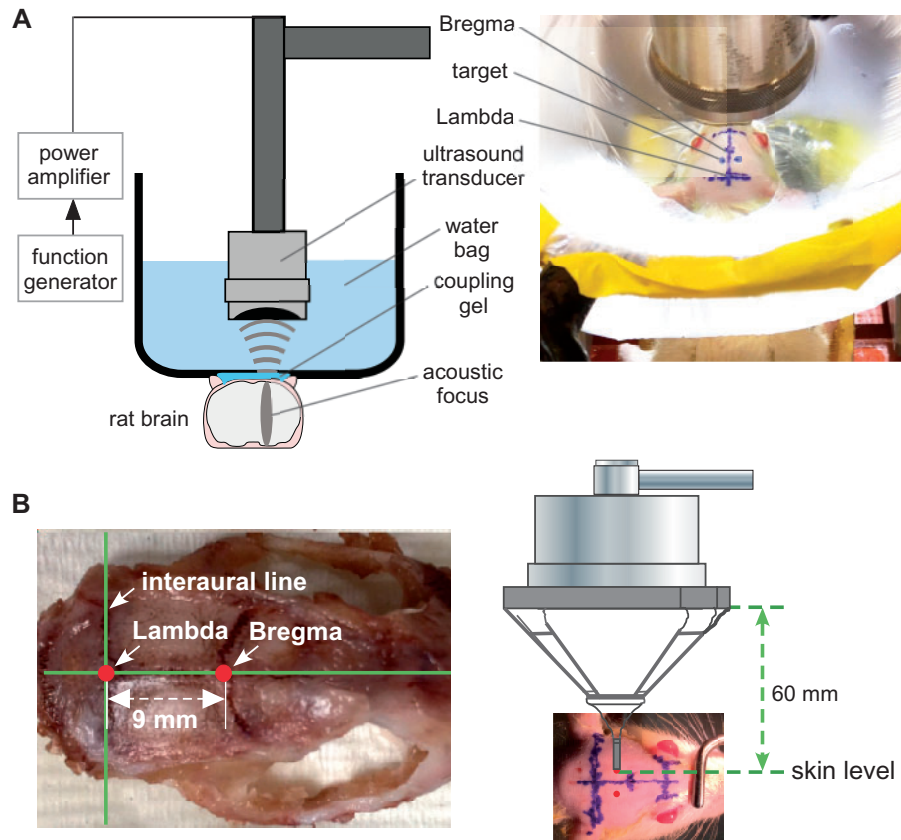


FIGURE 1. Experimental set-up for application of pulsed focused ultrasound and intravenous microbubbles for targeted permeabilization of the blood-brain barrier in rat. **(A)** Schematic (left) and photo (right) showing a rat immobilized on a stereotaxic frame, with ultrasound transducer and associated electronics for targeted ultrasound delivery through the intact skull from within a water bag coupled with ultrasound gel. **(B)** Determination of Bregma position (with skin intact) from interaural and sagittal lines (left), and pre-exposure ultrasound targeting using a guide cone with a tip for visual localization (right).

acoustic pressures of 0.3, 0.4, and 0.5 MPa in water were tested in initial dose-finding experiments. As markers of BBB permeability, 2% Evans blue dye (4 mL/kg body weight) and normal human IgG (hIgG, 5 mg/kg body weight) were injected intravenously at specified times following ultrasound exposure. Two hours later the rats were deeply anesthetized with an overdose of ketamine/xylazine and killed by transcardiac perfusion with heparinized saline containing 4% paraformaldehyde. The brains were collected for immunostaining and histology.

In some experiments the cervical spine from C4 to C6 at the dorsal midline was targeted to permeabilize the blood-spinal cord barrier. Anesthetized rats were immobilized on the stereotaxic frame as described above, and a custom support was positioned beneath the rat chest to flatten the spinal column from C2 to T2 for optimal exposure of the targeted C5 region. Microbubble administration and ultrasound exposure was done as described for brain above, except that a total exposure time of 4 minutes was used.

NMO Studies

Following dose-finding experiments, NMO studies were done using power settings for 0.5 MPa peak-negative acoustic

pressure in water, with 2-minute duration for brain and 4-minute duration for spinal cord. AQP4-IgG (5 mg/kg body weight) was administered via femoral vein catheter just after ultrasound exposure and rats were killed 5 days later. Brain or spinal cord was collected, sectioned, and imaged using fluorescence microscopy as described in Ref. (38). Control studies were done using AQP4 knockout rats, or using wild-type rats in which non-NMO human IgG was administered in place of AQP4-IgG, or using AQP4-IgG seropositive rats pre-treated with $Comp_{inh}$ to inhibit complement.

Immunofluorescence and H&E Staining

Frozen-sections (thickness 7 μ m) were immunostained as described in Ref. (41). Briefly, sections were incubated in blocking solution (1% BSA containing 0.3% Triton X-100 in PBS) for 1 hour at room temperature, then incubated overnight at 4°C with primary antibodies against albumin (1:100; MP Biomedicals, Santa Ana, CA), human IgG (1:200, Santa Cruz Biotechnology, Santa Cruz, CA), fibrinogen (1:100; Lifespan Bioscience, Seattle, WA), AQP4 (1:200, Santa Cruz Biotechnology), GFAP (1:200; Millipore), myelin basic protein ([MBP], 1:100, Santa Cruz Biotechnology), C5b-9 (1:100, Hycult Biotech, Wayne, PA), ionized calcium binding adaptor

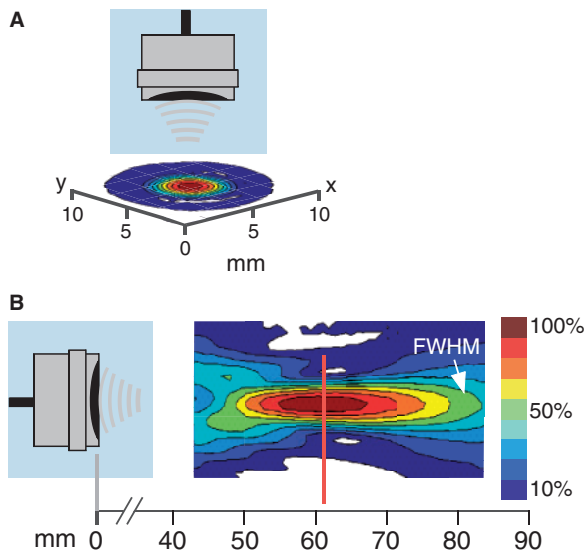


FIGURE 2. Acoustic pressure profiles of the focused ultrasound transducer measured in degassed water using a calibrated hydrophone within a 3D scanning system. Relative acoustic pressure distributions are shown in the transverse (A) and longitudinal (B) planes. The 50% contour delineates the full-width at half-maximum (FWHM) dimensions of the pressure distribution, with ~3.5 mm diameter and ~44 mm length. Parameters: 1 MHz, pulse width 10 ms, repetition rate 1 Hz.

molecule 1 (Iba-1; 1:400, Wako, Richmond, VA), or CD45 (1:50, Abcam, Cambridge, MA) followed by the appropriate species-specific Alexa Fluor-conjugated secondary antibody for 1 hour (5 µg/mL each, Invitrogen) at room temperature. Sections were mounted with Prolong Gold antifade reagent with DAPI (Invitrogen, Life Technologies, Eugene, OR) for visualization of immunofluorescence on a Leica fluorescence microscope or Nikon confocal microscope. Hematoxylin and eosin (H&E) staining on 7 µm of brain or cervical spinal cord sections was done using standard procedures.

Statistical Analysis

Data are presented as mean ± SEM. Statistical analysis was performed using Prism 5 GraphPad Software package (San Diego, CA). The normality of the data was established by Bartlett’s test for equal variances and a one-way ANOVA with Newmann-Keuls post-hoc test to compare groups.

RESULTS

Instrument Set-Up and Characterization of the Acoustic Field

The goal was to produce robust, transient permeabilization of the BBB at a defined location by ultrasound-induced stable microbubble cavitation without significant erythrocyte extravasation or inflammation. Experiments were done in rat brain in which the head was immobilized in a stereotaxic frame to deliver the ultrasound at defined coordinates. As diagrammed in Figure 1, the focal point of the ultrasound transducer was localized and aligned to the target region using a

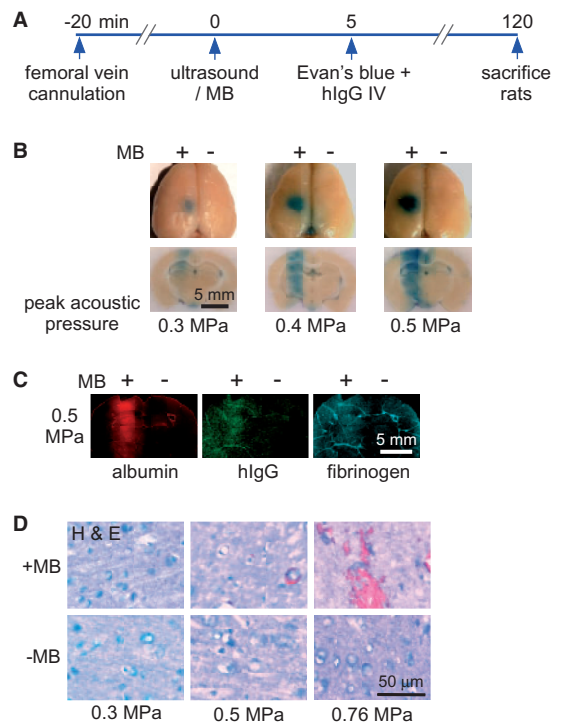


FIGURE 3. Blood-brain barrier permeabilization in rats following focused pulsed ultrasound. (A) Rats were exposed to ultrasound (1 MHz, pulse width 10 ms, repetition rate 1 Hz) for 2 minutes just after injection of a 100-µL bolus of Optison microbubbles (or vehicle control). Evan’s blue dye and human IgG were infused intravenously just after ultrasound exposure. (B) Photographs of Evan’s blue staining of rat brain surface and coronal brain sections at 120 minutes after ultrasound exposure at acoustic pressures of 0.3, 0.4, and 0.5 MPa, with and without microbubble infusion (on ipsilateral and contralateral hemispheres, respectively). (C) Immunofluorescence of albumin, human IgG, and fibrinogen. (D) Hematoxylin and eosin staining of brain sections, with positive control showing hemorrhage at 0.76 MPa. Data in B–D are representative of studies on 2–3 rats per group.

fabricated guide cone, which was replaced by a reservoir containing degassed water with ultrasound gel applied between the reservoir and skin of the rat head. An indwelling intravenous catheter allowed delivery of microbubbles just before application of ultrasound, and other materials at specified times following ultrasound exposure.

The spatial acoustic pressure distribution produced by the focused ultrasound was mapped using a hydrophone detector submerged in a degassed water tank along with the transducer. The pressure profile at the focal zone was an elongated ellipse with full width at half maximum of diameter ~3.5 mm and length ~44 mm. The spatial peak acoustic pressure profile in the transverse and longitudinal planes in water are shown in Figure 2. A similar energy deposition profile predicted in brain matter with significant attenuation of ~40% by the rat skull and spine is expected (37, 39) in a manner that recapitulated in vivo geometry.

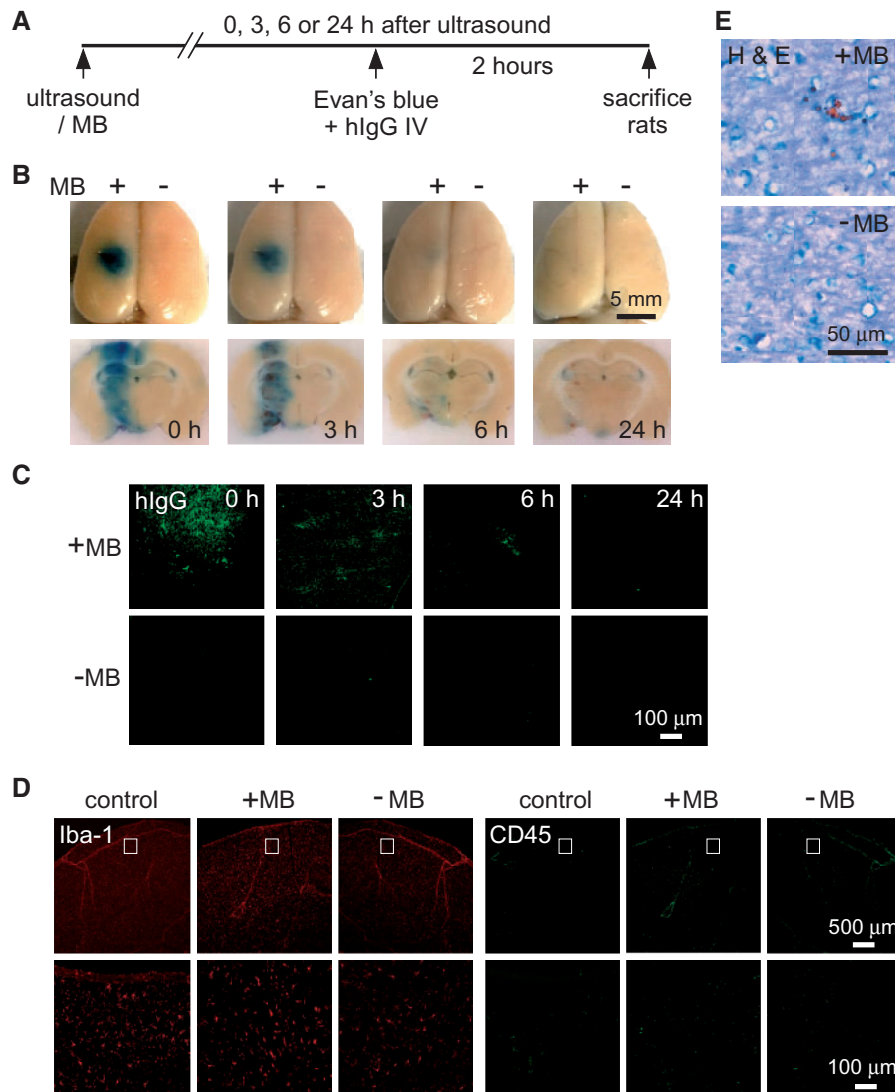


FIGURE 4. Kinetics of blood-brain barrier permeabilization following pulsed focused ultrasound. **(A)** Rats were treated as in Figure 3 (peak acoustic pressure 0.5 MPa), except that Evan’s blue dye and human IgG were infused at different times after ultrasound exposure and rats were killed 2 hours later. **(B)** Photographs of rat brain surface and coronal brain sections for indicated times between ultrasound exposure and animals’ death. **(C)** Human IgG immunofluorescence of brain sections at indicated times with or without microbubbles (MB). **(D)** Immunostaining for activated microglia (Iba-1) and leukocytes (CD45) at 24 hours after ultrasound exposure. **(E)** H&E staining at 24 hours after ultrasound exposure. Data in **B–E** are representative of studies on 2–3 rats per group.

BBB Permeabilization in Rats Following Pulsed Focused Ultrasound

A range of parameters (acoustic pressure, pulse width, exposure time) was tested initially using Evan’s blue dye extravasation as a visual indicator of BBB permeabilization (Fig. 3A). Photographs of the brain surface and coronal sections through the brain (Fig. 3B) show that Evan’s blue extravasation depends on peak acoustic pressure in a highly nonlinear manner and that its spatial profile was long and narrow as expected from the acoustic field profile in Figure 2. Evan’s blue extravasation was not seen without microbubble infusion. Immunofluorescence in Figure 3C shows that the

ultrasound produced extravasation of intravenously administered human IgG (molecular size ~150 kDa), and of endogenous serum albumin (~66 kDa), with lesser extravasation seen for fibrinogen (~340 kDa). H&E-stained sections showed minimal or no erythrocyte extravasation or inflammatory cell infiltration (Fig. 3D).

The kinetics of BBB permeabilization was determined by killing rats at different times after ultrasound and microbubble exposure, in which Evan’s blue and human IgG were administered 2 hours prior to death (Fig. 4A). Figure 4B shows Evan’s blue extravasation for up to 3 hours after ultrasound exposure, with much less extravasation seen at 6

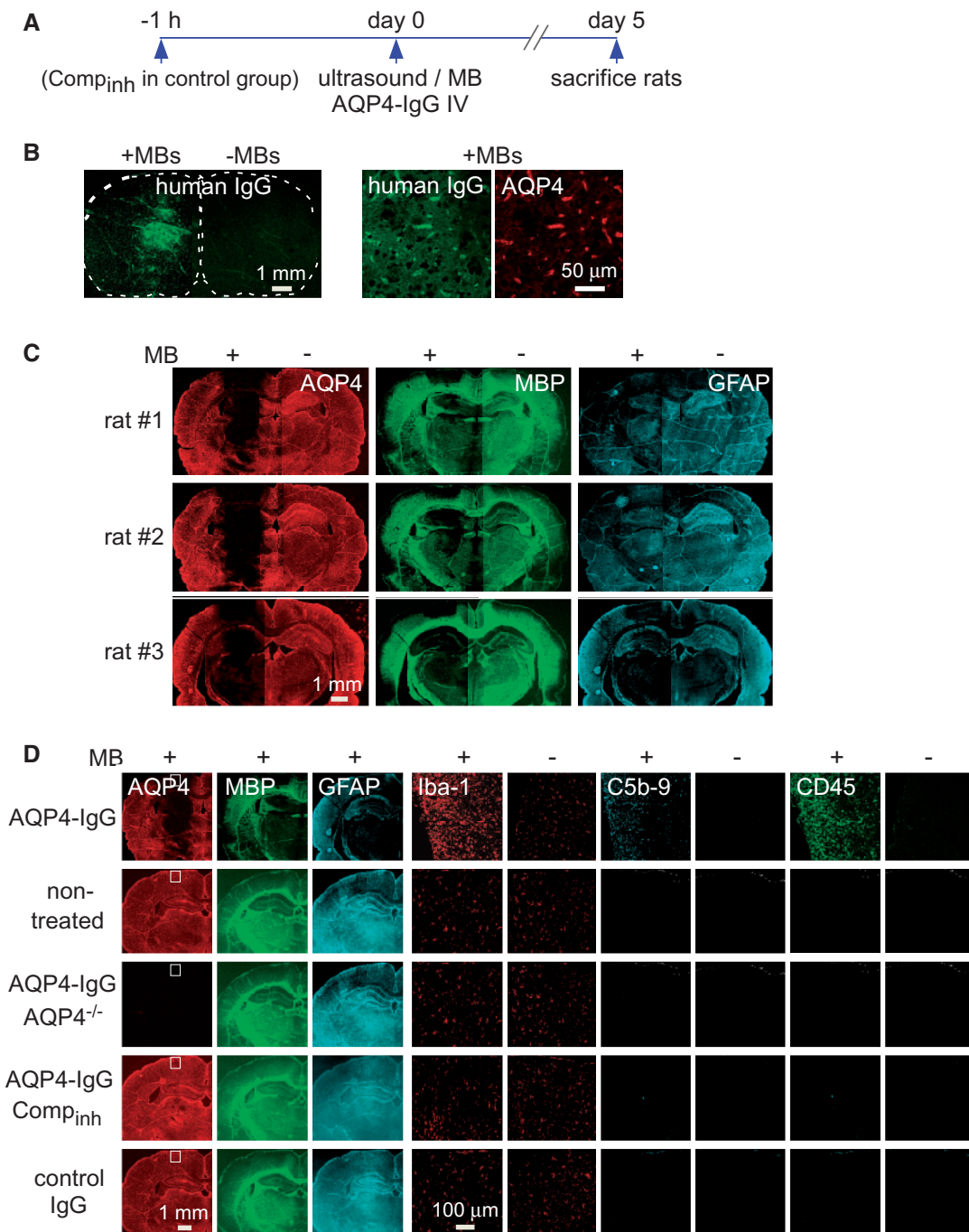


FIGURE 5. NMO pathology in seropositive rats following pulsed focused ultrasound. **(A)** Rats were exposed to focused ultrasound as in Figure 1, with AQP4-IgG (5 mg/kg body weight) infused intravenously just after ultrasound exposure. **(B)** AQP4-IgG localization in brain slices at 3 hours after exposure to focused ultrasound with peak acoustic pressure of 0.5 MPa for 2 minutes. **(C)** AQP4, GFAP, MBP immunofluorescence of brain sections in AQP4-IgG seropositive rats at day 5 after ultrasound exposure. Representative of studies on 4 rats per group. **(D)** Immunofluorescence of AQP4, MBP, GFAP, Iba-1, C5b-9, and CD45 in control studies including: nontreated rats, AQP4-IgG seropositive rats pretreated with complement inhibitor, rats given (non-NMO) IgG in place of AQP4-IgG, and seropositive AQP4^{-/-} rats. Representative of studies on 2–3 rats per group.

hours. A similar temporal pattern was seen for extravasation of human IgG (Fig. 4C). No significant inflammation or bleeding was seen at 24 hours after ultrasound exposure by

immunofluorescence for inflammatory cells (CD45) and activated microglial (Iba-1) (Fig. 4D), and H&E staining (Fig. 4E).

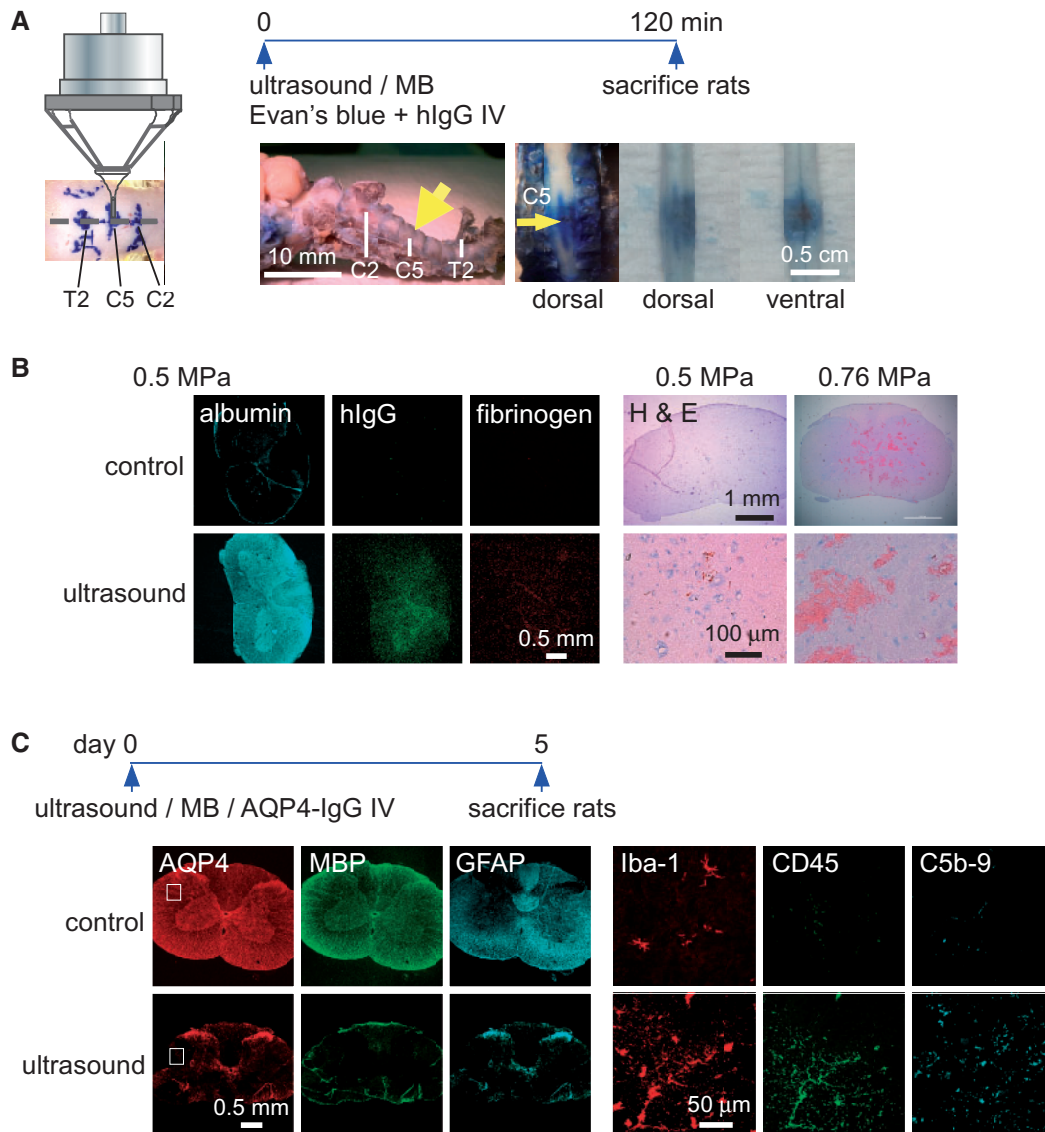


FIGURE 6. NMO pathology in cervical spinal cord of seropositive rats following pulsed focused ultrasound. **(A)** Experimental setup and photographs showing ultrasound target at C5 and Evan's blue extravasation in cervical spinal cord from C4 to C6 after ultrasound exposure (0.5 MPa peak acoustic pressure for 4 minutes). **(B)** Immunofluorescence of albumin, human IgG, and fibrinogen, and H&E staining with positive control of hemorrhage using 0.76 MPa acoustic pressure. **(C)** AQP4, GFAP, MBP, Iba-1, CD45, and C5b-9 immunofluorescence of cervical spinal cord in AQP4-IgG seropositive rats at 5 days after ultrasound exposure comparing with untreated control. Representative of studies on 3 rats per group.

NMO Pathology in Brain of Seropositive Rats Following Focused Pulsed Ultrasound

To produce NMO pathology in brain, ultrasound with microbubbles was applied to rats made seropositive for AQP4-IgG by intravenous injection of a well-characterized recombinant monoclonal human AQP4-IgG (Fig. 5A). Death of rats at 3 hours after ultrasound exposure showed deposition of the human recombinant AQP4-IgG in elongated elliptical pattern (Fig. 5B) similar to that seen for Evan's blue dye. To study NMO pathology, immunofluorescence of rat brain was done at 5 days after ultrasound exposure, staining for markers of astrocytes (AQP4 and GFAP), myelin (MBP), inflamma-

tion (Iba-1 and CD45), and activated complement (C5b-9). Figure 5C shows positive immunofluorescence for each of these markers in the brain hemisphere in which microbubbles were infused just prior to ultrasound exposure, but not in the contralateral hemisphere that was exposed to ultrasound but without microbubbles. An interesting observation was a greater loss of astrocytes and myelin in gray matter than in white matter.

Control studies were done to confirm that the NMO pathology required microbubble administration, complement, AQP4-IgG, and AQP4. As shown in Figure 5D, NMO pathology was not seen: (a) in the absence of microbubbles;

(b) when complement was inhibited by intravenous administration of Comp_{inh} ; (c) when (non-NMO) human IgG was infused in place of NMO-IgG; and (d) in AQP4-IgG seropositive AQP4^{-/-} rats.

NMO Pathology in Rat Spinal Cord

Similar studies were done in which the pulsed ultrasound was focused onto cervical spinal cord at the level of C5 in which the spinous processes are relatively shorter and flatter compared with thoracic or lumbar vertebrae, and in which there is little effect of respiration (Fig. 6A). Initial studies of ultrasound power requirement showed 0.76 MPa peak acoustic pressure in water caused marked hemorrhage at the targeted spot *in vivo*, where 0.5 MPa in water produced transient blood-spinal cord barrier opening, as seen by extravasation of Evan's blue (Fig. 6A), human IgG, albumin, and fibrinogen, with little erythrocyte extravasation (Fig. 6B). No extravasation of human IgG, albumin, or fibrinogen was seen in control rats not exposed to ultrasound.

Ultrasound exposure using 0.5 MPa peak acoustic pressure with microbubbles for 4 minutes in AQP4-IgG seropositive rats resulted in NMO pathology in spinal cord after 5 days. Immunostaining of cervical spinal cord showed loss of astrocyte markers, demyelination, inflammation, and deposition of activated complement (Fig. 6C), seen as spotty loss of AQP4, GFAP, and MBP, and staining for Iba-1, CD45, and activated complement C5b-9.

DISCUSSION

The results here establish the utility of pulsed focused ultrasound with stable microbubble cavitation to create NMO pathology in the CNS of AQP4-IgG seropositive rats, and demonstrate that transient BBB permeabilization is sufficient to produce NMO pathology. Characteristic pathological features of NMO, including astrocyte injury, inflammation, deposition of activated complement, and demyelination, were seen following exposure of AQP4-IgG seropositive rats to focused ultrasound with microbubbles, without inflammation, hemorrhage, or ischemia. NMO pathology was not seen without microbubbles, with administration of a complement inhibitor, when (non-NMO) human IgG was administered in place of NMO-IgG, or in AQP4-IgG seropositive AQP4^{-/-} rats. Our data support the conclusion that passive transfer of AQP4-IgG into the CNS can produce NMO pathology without underlying inflammation, sensitized T cells, or direct injury.

The ultrasound model established here advances the modeling of NMO pathogenesis using experimental animals. Prior rodent models of NMO involved administration of AQP4-IgG or NMO patient sera into the CNS by direct injection into brain or cerebrospinal space (18–23). Such models, though initially useful to demonstrate the pathogenicity of AQP4-IgG and for testing of some therapeutics, are nonphysiological. Other experimental animal models of NMO utilized rats made seropositive by systemic administration of AQP4-IgG or NMO patient sera. Whereas AQP4-IgG seropositive rats do not develop spontaneous NMO disease, some manifestations of NMO are seen following brain injury (25) or

creation of an inflammatory environment by experimental autoimmune encephalomyelitis (23, 28, 30, 42), infusion of activated T cells (6, 7, 9, 43), or infusion of cytokines (29). Another limitation of prior models has been the challenges in producing robust NMO pathology in spinal cord and optic nerve, the tissues that are most relevant to human NMO. The histopathology in NMO includes loss of AQP4 immunoreactivity, vasocentric deposition of IgG and activated complement, inflammatory cell infiltration, and demyelination, with ultimate neuronal loss. The pathological changes in brain and spinal cord found herein are characteristic of NMO pathology. The use of focused ultrasound with microbubbles allows spatially targeted creation of robust NMO pathology in AQP4-IgG seropositive rats without the need to cause injury or inflammation. Also, the creation of spatially defined pathology allows study of an internal negative control, such as the nonexposed brain, which is not possible with some prior models.

This study builds on a considerable body of prior work demonstrating the utility of focused ultrasound with stable microbubble cavitation to permeabilize capillary endothelial barriers. Noninvasive, reversible, transient, and regional opening of the BBB has been shown to facilitate targeted delivery of large therapeutic molecules into the CNS, including antibodies, growth factors, nanomedicine formulations, and therapeutic cells (44–48). Several preclinical studies support the safety of focused ultrasound with stable microbubble cavitation, which show minimal erythrocyte extravasation and inflammation under optimized conditions (35, 37, 44, 45, 49–51). Currently, phase I human clinical trials are in progress using focused ultrasound with microbubble cavitation to open the BBB for doxorubicin administration to brain tumors (NCT02343991), and for safety and effectiveness of the ultrasound device ExAblate Transcranial (220 kHz) System (NCT02986932) and the SONOCLOUD implantable medical device (NCT03119961) in early Alzheimer disease.

We note technical challenges and limitations of the methodology described herein. Precise targeting of the acoustic focal volume is needed, as is reproducibility of exposure conditions. Targeting was accomplished here using a removable 3D printed focus cone and stereotaxic methodology. Careful selection of parameters for ultrasound exposure, including acoustic pressure, pulse width and repetition rate, and total exposure time, is important to produce stable microbubble cavitation under the experimental conditions. Consistent intravenous delivery of the activated microbubble preparation immediately before ultrasound exposure is important as well. The inclusion of suitable standards and controls is important to ensure reproducibility, as well as evaluation of possible injury and inflammation in target tissues produced by ultrasound exposure. Further improvements to the methods establish here might include real-time monitoring of stable microbubble cavitation and permeabilization of the BBB (49, 52, 53). The use of ultrasound transducers with tighter focusing might be desirable for some more precise applications such as targeting the optic nerve.

In summary, the results here demonstrate the application of focused pulsed ultrasound with stable microbubble cavitation to allow entry of NMO autoantibody into brain and spinal

cord of AQP4-IgG seropositive rats to produce NMO pathology. The observation that transient permeabilization of the BBB alone, without inflammation, immunomodulation, or injury, is sufficient to produce NMO pathology in seropositive rats addresses a long-standing question in the field. Future applications of ultrasound with microbubble cavitation in the NMO field may include investigation of novel disease pathogenesis mechanisms and therapeutics, generation of nonrodent experimental animal models of NMO, and delivery of biologic and cell therapeutics such as neural stem cells.

ACKNOWLEDGMENT

We thank Dr Jeffrey Bennett (Univ. Colorado Denver, Aurora, CO) for providing recombinant monoclonal NMO antibody.

REFERENCES

- Lennon VA, Kryzer TJ, Pittock SJ, et al. IgG marker of optic-spinal multiple sclerosis binds to the aquaporin-4 water channel. *J Exp Med* 2005; 202:473–7
- Jarius S, Wildemann B. AQP4 antibodies in neuromyelitis optica diagnostic and pathogenetic relevance. *Nat Rev Neurol* 2010;6:383–92
- Fujihara K. Neuromyelitis optica and astrocytic damage in its pathogenesis. *J Neurol Sci* 2011;306:183–7
- Papadopoulos MC, Verkman AS. Aquaporin 4 and neuromyelitis optica. *Lancet Neurol* 2012;11:535–44
- Tradtrantip L, Felix CM, Spirig R, et al. Recombinant IgG1 Fc hexamers block cytotoxicity and pathological changes in experimental in vitro and rat models of neuromyelitis optica. *Neuropharmacology* 2018;133:345–53
- Zeka B, Hastermann M, Hochmeister S, et al. Highly encephalitogenic aquaporin 4-specific T cells and NMO-IgG jointly orchestrate lesion location and tissue damage in the CNS. *Acta Neuropathol* 2015;130:783–98
- Sagan SA, Winger RC, Cruz-Herranz A, et al. Tolerance checkpoint bypass permits emergence of pathogenic T cells to neuromyelitis optica autoantigen aquaporin-4. *Proc Natl Acad Sci USA* 2016;113:14781–6
- Ratelade J, Asavapanumas N, Ritchie AM, et al. Involvement of antibody-dependent cell-mediated cytotoxicity in inflammatory demyelination in a mouse model of neuromyelitis optica. *Acta Neuropathol* 2013;126:699–709
- Pohl M, Fischer MT, Mader S, et al. Pathogenic T cell responses against aquaporin 4. *Acta Neuropathol* 2011;122:21–34
- Tradtrantip L, Yao X, Su T, et al. Bystander mechanism for complement-initiated early oligodendrocyte injury in neuromyelitis optica. *Acta Neuropathol* 2017;134:35–44
- Papadopoulos MC, Bennett JL, Verkman AS. Treatment of neuromyelitis optica: State-of-the-art and emerging therapies. *Nat Rev Neurol* 2014;10:493–506
- Bradl M, Lassmann H. Experimental models of neuromyelitis optica. *Brain Pathol* 2014;24:74–82
- Li M, Yan Y. Experimental models of neuromyelitis optica: Current status, challenges and future directions. *Neurosci Bull* 2015;31:735–44
- Jones MV, Collongues N, de Seze J, et al. Review of animal models of neuromyelitis optica. *Mult Scler Relat Disord* 2012;1:174–9
- Stimmer L, Fovet CM, Serguera C. Experimental models of autoimmune demyelinating diseases in nonhuman primates. *Vet Pathol* 2018;55:27–41
- Roemer SF, Parisi JE, Lennon VA, et al. Pattern-specific loss of aquaporin-4 immunoreactivity distinguishes neuromyelitis optica from multiple sclerosis. *Brain* 2007;130:1194–205
- Jarius S, Wildemann B, Paul F. Neuromyelitis optica: Clinical features, immunopathogenesis and treatment. *Clin Exp Immunol* 2014;176:149–64
- Saadoun S, Waters P, Bell BA, et al. Intra-cerebral injection of neuromyelitis optica immunoglobulin G and human complement produces neuromyelitis optica lesions in mice. *Brain* 2010;133:349–61
- Marignier R, Ruiz A, Cavagna S, et al. Neuromyelitis optica study model based on chronic infusion of autoantibodies in rat cerebrospinal fluid. *J Neuroinflamm* 2016;13:111
- Asavapanumas N, Ratelade J, Verkman AS. Unique neuromyelitis optica pathology produced in naive rats by intracerebral administration of NMO-IgG. *Acta Neuropathol* 2014;127:539–51
- Zhang H, Verkman AS. Eosinophil pathogenicity mechanisms and therapeutics in neuromyelitis optica. *J Clin Invest* 2013;123:2306–16
- Zhang H, Verkman AS. Longitudinally extensive NMO spinal cord pathology produced by passive transfer of NMO-IgG in mice lacking complement inhibitor CD59. *J Autoimmun* 2014;53:67–77
- Wrzoc C, Winkler A, Metz I, et al. Early loss of oligodendrocytes in human and experimental neuromyelitis optica lesions. *Acta Neuropathol* 2014;127:523–38
- Geis C, Ritter C, Ruschil C, et al. The intrinsic pathogenic role of autoantibodies to aquaporin 4 mediating spinal cord disease in a rat passive-transfer model. *Exp Neurol* 2015;265:8–21
- Asavapanumas N, Verkman AS. Neuromyelitis optica pathology in rats following intraperitoneal injection of NMO-IgG and intracerebral needle injury. *Acta Neuropathol Commun* 2014;2:48
- Ratelade J, Bennett JL, Verkman AS. Intravenous neuromyelitis optica autoantibody in mice targets aquaporin-4 in peripheral organs and area postrema. *PLoS One* 2011;6:e27412
- Nishiyama S, Ito T, Misu T, et al. A case of NMO seropositive for aquaporin-4 antibody more than 10 years before onset. *Neurology* 2009; 72:1960–1
- Bennett JL, Lam C, Kalluri SR, et al. Intrathecal pathogenic anti-aquaporin-4 antibodies in early neuromyelitis optica. *Ann Neurol* 2009; 66:617–29
- Kitic M, Hochmeister S, Wimmer I, et al. Intrastratial injection of interleukin-1 beta triggers the formation of neuromyelitis optica-like lesions in NMO-IgG seropositive rats. *Acta Neuropathol Commun* 2013; 1:5
- Bradl M, Misu T, Takahashi T, et al. Neuromyelitis optica: Pathogenicity of patient immunoglobulin in vivo. *Ann Neurol* 2009;66:630–43
- McDannold N, Arvanitis CD, Vykhodtseva N, et al. Temporary disruption of the blood-brain barrier by use of ultrasound and microbubbles: Safety and efficacy evaluation in rhesus macaques. *Cancer Res* 2012;72:3652–63
- Samiotaki G, Konofagou EE. Dependence of the reversibility of focused-ultrasound-induced blood-brain barrier opening on pressure and pulse length in vivo. *IEEE Trans Ultrason Ferroelectr Freq Control* 2013;60:2257–65
- O'Reilly MA, Waspe AC, Ganguly M, et al. Focused-ultrasound disruption of the blood-brain barrier using closely-timed short pulses: Influence of sonication parameters and injection rate. *Ultrasound Med Biol* 2011; 37:587–94
- Marty B, Larrat B, Van Landeghem M, et al. Dynamic study of blood-brain barrier closure after its disruption using ultrasound: A quantitative analysis. *J Cereb Blood Flow Metab* 2012;32:1948–58
- Kobus T, Vykhodtseva N, Pilatou M, et al. Safety validation of repeated blood-brain barrier disruption using focused ultrasound. *Ultrasound Med Biol* 2016;42:481–92
- Weber-Adrian D, Thevenot E, O'Reilly MA, et al. Gene delivery to the spinal cord using MRI-guided focused ultrasound. *Gene Ther* 2015;22:568–77
- Payne AH, Hawryluk GW, Anzai Y, et al. Magnetic resonance imaging-guided focused ultrasound to increase localized blood-spinal cord barrier permeability. *Neural Regen Res* 2017;12:2045–9
- Yao X, Verkman AS. Marked central nervous system pathology in CD59 knockout rats following passive transfer of neuromyelitis optica immunoglobulin G. *Acta Neuropathol Commun* 2017;5:15
- O'Reilly MA, Muller A, Hynynen K. Ultrasound insertion loss of rat parietal bone appears to be proportional to animal mass at submegahertz frequencies. *Ultrasound Med Biol* 2011;37:1930–7
- Paxinos G, Watson C. *The Rat Brain in Stereotaxic Coordinates*, 6th ed. Amsterdam; Boston: Academic Press/Elsevier 2007

41. Yao X, Verkman AS. Complement regulator CD59 prevents peripheral organ injury in rats made seropositive for neuromyelitis optica immunoglobulin G. *Acta Neuropathol Commun* 2017;5:57
42. Saini H, Rifkin R, Gorelik M, et al. Passively transferred human NMO-IgG exacerbates demyelination in mouse experimental autoimmune encephalomyelitis. *BMC Neurol* 2013;13:104
43. Pohl M, Kawakami N, Kitic M, et al. T cell-activation in neuromyelitis optica lesions plays a role in their formation. *Acta Neuropathol Commun* 2013;1:85
44. Dasgupta A, Liu M, Ojha T, et al. Ultrasound-mediated drug delivery to the brain: Principles, progress and prospects. *Drug Discov Today Technol* 2016;20:41–8
45. Poon C, McMahan D, Hynynen K. Noninvasive and targeted delivery of therapeutics to the brain using focused ultrasound. *Neuropharmacology* 2017;120:20–37
46. Burgess A, Ayala-Grosso CA, Ganguly M, et al. Targeted delivery of neural stem cells to the brain using MRI-guided focused ultrasound to disrupt the blood-brain barrier. *PLoS One* 2011;6:e27877
47. Park J, Aryal M, Vykhodtseva N, et al. Evaluation of permeability, doxorubicin delivery, and drug retention in a rat brain tumor model after ultrasound-induced blood-tumor barrier disruption. *J Control Release* 2017;250:77–85
48. Liu M, Jevtic S, Markham-Coultes K, et al. Investigating the efficacy of a combination Aβ-targeted treatment in a mouse model of Alzheimer's disease. *Brain Res* 2018;1678:138–45
49. Konofagou EE. Optimization of the ultrasound-induced blood-brain barrier opening. *Theranostics* 2012;2:1223–37
50. Fan CH, Lin CY, Liu HL, et al. Ultrasound targeted CNS gene delivery for Parkinson's disease treatment. *J Control Release* 2017;261:246–62
51. McMahan D, Hynynen K. Acute inflammatory response following increased blood-brain barrier permeability induced by focused ultrasound is dependent on microbubble dose. *Theranostics* 2017;7:3989–4000
52. Arvanitis CD, Livingstone MS, Vykhodtseva N, et al. Controlled ultrasound-induced blood-brain barrier disruption using passive acoustic emissions monitoring. *PLoS One* 2012;7:e45783
53. Chu PC, Chai WY, Tsai CH, et al. Focused ultrasound-induced blood-brain barrier opening: Association with mechanical index and cavitation index analyzed by Dynamic contrast-enhanced magnetic-resonance imaging. *Sci Rep* 2016;6:33264